

Spin-dependent dark matter interactions at loop-level in Ar and Xe

Nassim Bozorgnia,^{a,b} Muping Chen,^c Graciela B. Gelmini,^d Alvine C. Kamaha,^d and Yongheng Xu^d

^aDepartment of Physics, University of Alberta,
Edmonton, Alberta T6G 2E1, Canada

^bTheoretical Physics Institute, University of Alberta,
Edmonton, Alberta T6G 2E1, Canada

^cWPI-QUP, KEK, Oho 1-1, Tsukuba, Ibaraki 305-0801, Japan

^dDepartment of Physics and Astronomy, UCLA,
475 Portola Plaza, Los Angeles, CA 90095, USA

E-mail: nbozorgnia@ualberta.ca, mpchen@post.kek.jp, gelmini@physics.ucla.edu,
akamaha@physics.ucla.edu, xuyongheng@physics.ucla.edu

Abstract. Xenon and argon are the two noble gases used in tonne scale dark matter direct detection experiments. We compare the detection capability of both target elements for interactions due to a pseudoscalar mediator including loop-level contributions to the cross section. At tree-level this type of interaction depends on the nuclear spin and would thus not be detectable in argon-based detectors, since Ar has spin zero. However, at the loop-level the same interaction yields spin-independent contributions that would be detectable in an argon target and are not negligible with respect to the tree-level interactions in xenon, because these are momentum suppressed. In fact, the loop-level contributions are also important for xenon-based experiments at low recoil energies, which could change their discovery reach for this interaction.

Contents

1	Introduction	1
2	The interaction model	2
3	Loop-level corrections	3
4	Direct detection rates	4
5	Comparison of Ar and Xe detection capability	6
6	Conclusions	11

1 Introduction

Direct dark matter (DM) detection attempts to detect the energy deposited by the collision of a DM particle from the dark halo of our galaxy within a detector. Xenon (see e.g. [1–8]) and argon (see e.g. [9–14]) are the two liquefied noble gases used in tonne scale direct detection experiments. The proposed 40 tonne (50 tonne total) DARWIN [15], 60 tonne (75 tonne total) XLZD [7, 8] and 43 tonne (47 tonne total) PandaX-xT [6] DM direct detection experiments with liquid xenon, and 300 tonne Global Argon Dark Matter Collaboration (GADMC) consortium ARGO detector [16, 17] with liquid argon, will reach the sensitivity at which the interactions from coherent elastic neutrino-nucleus scattering – the “neutrino fog” – will become the most important background.

The best search strategy in direct DM detection is to cast as wide a net as possible in terms of DM-nucleus interactions (see e.g. ref. [18]). Because the argon nucleus does not have spin, argon-based direct detection experiments are insensitive to all interactions coupling the DM particle to nuclear spin, such as those with axial vector or pseudoscalar mediators at tree-level. Xenon is instead sensitive to these interactions. It is thus important to understand how much of a disadvantage argon-based detectors have with respect to those that are xenon-based to detect this type of interactions. The same interactions that lead to a nuclear spin-dependent cross section at tree-level, at the loop-level always contain terms that are independent of the nuclear spin, and could thus be detected in argon.

Loop-level corrections must include all the particles that can be exchanged within the loop given a particular particle model, and not only the main mediator that is usually sufficient to compute tree-level interactions. These corrections can be computed in a straightforward manner in UV complete particle models. However, we would like instead to extend as little as possible a simplified model consisting of the DM particle and its mediator, the elements needed for tree-level calculations, to preserve its generality. Several calculations exist in this spirit of loop-level corrections to the interactions mediated by a pseudoscalar particle [19–23]. This type of interaction is particularly favorable to produce sizable loop-level contributions to the interaction rate at low recoil energies because at tree-level the cross section is momentum transfer suppressed (see e.g. table 1 and eqs. (2.31) and (2.33) of ref. [18]). Using these loop-level calculations, here we compare the argon and xenon-based direct detection capabilities of fermionic DM with interactions mediated by a pseudoscalar boson with tree-level couplings $f\gamma_5 f$ with Standard Model (SM) fermions f .

The paper is structured as follows. In section 2 we discuss the general interaction model for the DM particle and the SM fermions. In section 3 we discuss the loop-level corrections to the interactions. In section 4 we present the expressions used for the computation of direct detection event rates. In section 5 we present our results on the detection capability of Ar and Xe-based detectors, and we conclude in section 6.

2 The interaction model

Models of DM particles with a pseudoscalar mediator have been studied for more than a decade [24–26], and UV complete models including interaction of this type have been studied at colliders (see e.g. [27–32]).

Loop-level contributions to a cross section depend on all the particles that can be exchanged in a particular theory, not only on the mediator which dominates the interaction at the tree-level. Thus, without postulating a complete model, it is of particular importance at this level to include the necessary couplings of the pseudoscalar mediator to the SM Higgs boson required by gauge invariance [19–23]. When these are included, even working at one-loop level, two-loop diagrams cannot be neglected [22, 23].

Following ref. [23], we assume here a simple model for the interaction of a Dirac fermion DM particle χ and SM fermions f mediated by a spin-zero boson field ϕ with mass m_ϕ . Two different types of Lagrangian terms are assumed: S-PS and PS-PS. Here, the first S (scalar) or PS (pseudoscalar) refers to the DM coupling without or with a γ_5 , respectively, and the second PS to the SM fermion coupling with a γ_5 . These are respectively

$$\mathcal{L}_{\text{S-PS}} = g_\chi \phi \bar{\chi} \chi + g_{\text{SM}} \sum_f \frac{m_f}{v} \phi \bar{f} i \gamma_5 f, \quad (2.1)$$

and

$$\mathcal{L}_{\text{PS-PS}} = g_\chi \phi \bar{\chi} i \gamma_5 \chi + g_{\text{SM}} \sum_f \frac{m_f}{v} \phi \bar{f} i \gamma_5 f, \quad (2.2)$$

where $v = 246 \text{ GeV}$ is the electroweak vacuum expectation value, g_χ and $(g_{\text{SM}} m_f/v)$ denote the coupling constants of the mediator ϕ to the DM and SM fermions, respectively, and m_f are the SM fermion masses. The couplings of the new field ϕ to SM fermions are taken to be proportional to the Yukawa-couplings (m_f/v) , in agreement with the hypothesis of minimal flavour violation [33], which leads to weakened flavor physics constraints on them.

Gauge symmetry requires that ϕ couples to the SM Higgs field in a quartic term in the scalar potential. After the electroweak spontaneous symmetry breaking, this quartic coupling yields the term

$$\mathcal{L}_{\text{int}}^{\text{Higgs}} = \frac{1}{2} \lambda_{\phi h} v h \phi^2, \quad (2.3)$$

where h is the Higgs boson field. This term is identified in ref. [23] as the most relevant ϕ - h coupling, because other interaction terms involving two Higgs bosons do not give any relevant contribution to the calculation of direct detection signatures. The constant $\lambda_{\phi h}$ is an additional free parameter of the model, constrained to be $\lambda_{\phi h} \lesssim 0.01$ when the invisible decays $h \rightarrow \phi\phi$ are kinematically possible, i.e. when $m_\phi < m_h/2$ (see figure 6 of ref. [23]).

The parameters of this simple model are, therefore, five: the mass of the DM particle m_χ , the mass of the mediator m_ϕ , and the three coupling constants g_χ, g_{SM} and $\lambda_{\phi h}$. As explained below, in the following m_ϕ is taken to be smaller than the t quark mass and larger than the b quark mass, $m_b < m_\phi \ll m_t$, for consistency of the calculations [23].

Initial	Effective S-S	Effective PS-S	Effective S-PS	Effective PS-PS
S-PS	X	0	X	X
PS-PS	X	X	X	X

Table 1. The two initial couplings in eqs. (2.1) and (2.2), shown in the first column, generate at the loop-level an effective low energy Lagrangian with terms proportional to some of the other interactions indicated by an X [23]. S-S refers to couplings $(\bar{\chi}\chi\bar{f}f)$ and PS-S to $(\bar{\chi}\gamma_5\chi\bar{f}f)$, which are both independent of the nuclear spin.

3 Loop-level corrections

The two initial interactions in eqs. (2.1) and (2.2), given in the first column of table 1, generate at the loop-level an effective low energy Lagrangian which contains terms proportional to some of the other possible interactions [23], indicated by an X in the table. S-S refers to couplings $[\bar{\chi}\chi\bar{f}f]$ and PS-S to $[\bar{\chi}\gamma_5\chi\bar{f}f]$, which are both independent of the nuclear spin. Namely, at the loop-level S-PS interactions generate S-S, S-PS and PS-PS terms, while starting from PS-PS interactions, terms proportional to all four interaction types are produced at the loop-level.

We utilize the effective approach developed in ref. [23] for calculations of two-loop processes contributing to the effective DM-gluon interactions, which can replace the full two-loop calculations. In this approach, the two-loop processes can be decomposed into two one-loop diagrams by first integrating out the top quark, and then the mediator ϕ . In order to apply this approach, we need to take $m_\phi \ll m_t$. In this case, ref. [23] shows that their effective approach for the two-loop calculation agrees very well with the full two-loop calculations for all values of m_χ (see figure 4 of ref. [23]), and also that when $m_\phi > m_b$ the contribution from bottom and charm quarks can be neglected.¹

After matching the effective DM-quark and effective DM-gluon interactions onto non-relativistic DM-nucleon interactions, the effective Lagrangian can be written as [23],

$$\mathcal{L}_{\chi N}^{\text{eff}} = \left(\mathcal{C}_{\text{eff},N}^{\text{SI}} \bar{\chi}\chi + \mathcal{C}_{\text{eff},N}^{\text{SI,CPV}} \bar{\chi}i\gamma_5\chi \right) \bar{N}N + \left(\mathcal{C}_{\text{eff},N}^{\text{SD,CPV}} \bar{\chi}\chi + \mathcal{C}_{\text{eff},N}^{\text{SD}} \bar{\chi}i\gamma_5\chi \right) \bar{N}i\gamma_5N, \quad (3.1)$$

where $N = p, n$ indicates proton or neutron fields. The coefficients $\mathcal{C}_{\text{eff},N}$ are given in ref. [23] and depend on tree-level and loop-level coefficients. The labels “SI” and “SD” refer to nuclear-spin dependent and nuclear-spin independent terms, and the label “CPV” refers to CP violation and is used for coefficients that exist only when CP is violated.

We refer the reader to ref. [23] for detailed expressions of the $\mathcal{C}_{\text{eff},N}$ coefficients, and only mention here their dependence on the Passarino-Veltman functions C_0 and C_2 [35], as well as the X_2 , Y_2 , and Z functions defined in ref. [36],

$$\begin{aligned} \mathcal{C}_{\text{eff},N}^{\text{SI}} &= \mathcal{C}_{\text{eff},N}^{\text{SI}}(\mathcal{C}^{\text{tree}}, C_0, C_2, X_2, Y_2, Z_{00}, Z_{001}, Z_{111}), \\ \mathcal{C}_{\text{eff},N}^{\text{SI,CPV}} &= \mathcal{C}_{\text{eff},N}^{\text{SI,CPV}}(\mathcal{C}^{\text{tree}}, C_0, X_2, Z_{00}, Z_{11}), \\ \mathcal{C}_{\text{eff},N}^{\text{SD}} &= \mathcal{C}_{\text{eff},N}^{\text{SD}}(\mathcal{C}^{\text{tree}}, C_0, X_2), \\ \mathcal{C}_{\text{eff},N}^{\text{SD,CPV}} &= \mathcal{C}_{\text{eff},N}^{\text{SD,CPV}}(\mathcal{C}^{\text{tree}}, C_0, C_2, X_2, Y_2), \end{aligned} \quad (3.2)$$

¹Loop processes for $m_\phi \gg m_t$, and more general electroweak structures, were calculated in ref. [34].

where

$$\mathcal{C}^{\text{tree}} = \frac{g_\chi g_{\text{SM}}}{vm_\phi^2}. \quad (3.3)$$

For the on-shell condition $p^2 = m_\chi^2$, where p is the DM particle momentum, the functions C_0 , C_2 , X_2 , Y_2 , as well as the Z functions, only depend on m_χ and m_ϕ , and can be calculated using `Package-X` [37, 38] and `CollierLink` [39] (see also appendix A of ref. [23]). Notice that the $\mathcal{C}_{\text{eff},N}$ coefficients also depend on the nuclear form factors for the quark and gluon contents of the nucleon. For the SD coefficients, the nuclear form factors depend on the momentum $q = |\vec{q}|$ exchanged between the DM particle and the nucleon, due to contributions from the π and η mesons [40].²

In general, the SI coefficients $\mathcal{C}_{\text{eff},N}^{\text{SI}}$ and $\mathcal{C}_{\text{eff},N}^{\text{SI,CPV}}$ depend on the five parameters m_χ , m_ϕ , g_χ , g_{SM} , and $\lambda_{\phi h}$. The SD coefficients $\mathcal{C}_{\text{eff},N}^{\text{SD}}$ and $\mathcal{C}_{\text{eff},N}^{\text{SD,CPV}}$ depend on those same parameters in addition to the momentum transfer q .

The effective Lagrangian in eq. (3.1) can be parametrized in terms of a set of effective operators in the non-relativistic limit [42–46],

$$\mathcal{L}_{\chi N}^{\text{eff}} \rightarrow \sum_i c_i^N \mathcal{O}_i^N. \quad (3.4)$$

For the model we are considering, only the following four effective operators contribute,

$$\begin{aligned} \mathcal{O}_1^N &= 1_\chi 1_N, \\ \mathcal{O}_6^N &= \left(\vec{S}_\chi \cdot \frac{\vec{q}}{m_N} \right) \left(\vec{S}_N \cdot \frac{\vec{q}}{m_N} \right), \\ \mathcal{O}_{10}^N &= i \vec{S}_N \cdot \frac{\vec{q}}{m_N}, \\ \mathcal{O}_{11}^N &= i \vec{S}_\chi \cdot \frac{\vec{q}}{m_N}, \end{aligned} \quad (3.5)$$

where \vec{S}_χ is the DM particle spin, \vec{S}_N is the nucleon spin, and m_N is the nucleon mass. The coefficients corresponding to these operators are respectively $c_1^N = \mathcal{C}_{\text{eff},N}^{\text{SI}}$, $c_6^N = (m_N/m_\chi) \mathcal{C}_{\text{eff},N}^{\text{SD}}$, $c_{10}^N = \mathcal{C}_{\text{eff},N}^{\text{SD,CPV}}$, and $c_{11}^N = -(m_N/m_\chi) \mathcal{C}_{\text{eff},N}^{\text{SI,CPV}}$.

4 Direct detection rates

With the operators given in eq. (3.5), we calculate the spin averaged DM-nuclide, T , transition probability [45],

$$P_{\text{tot},T} = \frac{1}{2j_\chi + 1} \frac{1}{2j_T + 1} \sum_{\text{spins}} |\mathcal{M}_T|^2, \quad (4.1)$$

where j_χ and j_T are the total angular momentum of the DM and the target nucleus respectively and \mathcal{M}_T is the DM-nucleus scattering amplitude summed over nucleons and computed between nuclear states (defined e.g. in eq. (40) of ref. [45]). This transition probability is then used to calculate the DM-nucleus differential cross-section,

$$\frac{d\sigma_T}{dE_R} = \frac{m_T}{2\pi v^2} P_{\text{tot},T} \quad (4.2)$$

²Updated nuclear form factors have been very recently given in ref. [41].

where E_R denotes the recoil energy of the target nucleus, m_T is the mass of the target nucleus, and \vec{v} is the relative velocity between the DM and the target nucleus, with $v \equiv |\vec{v}|$. Throughout our calculations, we assume that there is no difference between the recoil energy and the observed energy; therefore, we do not consider an experimental energy resolution.

In the case that the detector includes multiple nuclides, the differential event rate per unit energy, detector mass, and time is given by

$$\frac{dR}{dE_R} = \sum_T \frac{dR_T}{dE_R} = \sum_T \frac{C_T}{m_T} \frac{\rho_\chi}{m_\chi} \int_{v \geq v_{\min, T}} d^3v \frac{d\sigma_T}{dE_R} v f(\vec{v}, t), \quad (4.3)$$

where the sum is over the different isotopes or target nuclides, T , present in the detector, C_T is the mass fraction of T in the detector, ρ_χ is the local DM density, and $f(\vec{v}, t)$ is the local DM velocity distribution in the Earth's rest frame. The minimum DM speed to produce a recoil energy E_R in the detector is

$$v_{\min, T} = \frac{q}{2\mu_T} = \sqrt{\frac{m_T E_R}{2\mu_T^2}}, \quad (4.4)$$

where μ_T is the DM-target nucleus reduced mass.

We assume the Standard Halo Model [47] for describing the local distribution of DM in the galactic halo. Recent cosmological simulations including both DM and baryons show that the Maxwellian distribution fits well the local DM velocity distribution of Milky Way-like galaxies [48–51]. However, DM from massive satellites such as the Large Magellanic Cloud can significantly impact the high speed tail of the local DM velocity distribution [52–55]. For simplicity, we neglect these effects in this work.

The local DM density is set to $\rho_\chi = 0.3 \text{ GeV/cm}^3$. The local DM velocity distribution is modelled as a Maxwell-Boltzmann distribution in the galactic rest frame, and truncated at the local escape speed, v_{esc} , from the galaxy,

$$f_{\text{gal}}(\vec{v}) = \frac{1}{N_{\text{esc}}(v_0\sqrt{\pi})^3} \left[e^{-v^2/v_0^2} - e^{-v_{\text{esc}}^2/v_0^2} \right] \Theta(v_{\text{esc}}^2 - v^2), \quad (4.5)$$

where

$$N_{\text{esc}} = \text{erf}(v_{\text{esc}}/v_0) - \frac{2}{\sqrt{\pi}} \left(\frac{v_{\text{esc}}}{v_0} \right) e^{-v_{\text{esc}}^2/v_0^2} \left[1 + \frac{2}{3} \left(\frac{v_{\text{esc}}}{v_0} \right)^2 \right]. \quad (4.6)$$

Here, v_0 is the local circular speed, and the velocity distribution is normalized such that $\int d^3v f_{\text{gal}}(\vec{v}) = 1$. The second term in the bracket in eq. (4.5) ensures that the velocity distribution falls off smoothly to zero at v_{esc} . We take $v_0 = 235 \text{ km/s}$ based on measurements of galactic masers [56, 57], and $v_{\text{esc}} = 550 \text{ km/s}$ based on measurements of high velocity stars from the RAVE survey [58].

We transform the DM velocity distribution from the galactic rest frame to the Earth's rest frame,

$$f(\vec{v}, t) = f_{\text{gal}}(\vec{v} + \vec{v}_s + \vec{v}_e(t)), \quad (4.7)$$

where $\vec{v}_s = \vec{v}_c + \vec{v}_{\text{pec}}$ is the velocity of the Sun in the Galactic rest frame, and $\vec{v}_e(t)$ is Earth's velocity with respect to the Sun, which we neglect in this work. Here, \vec{v}_c is the Sun's circular velocity (where we take $v_c = v_0 = 235 \text{ km/s}$), and $\vec{v}_{\text{pec}} = (11.10, 12.24, 7.25) \text{ km/s}$ [59] is the peculiar velocity of the Sun with respect to the Local Standard of Rest, in galactic coordinates.

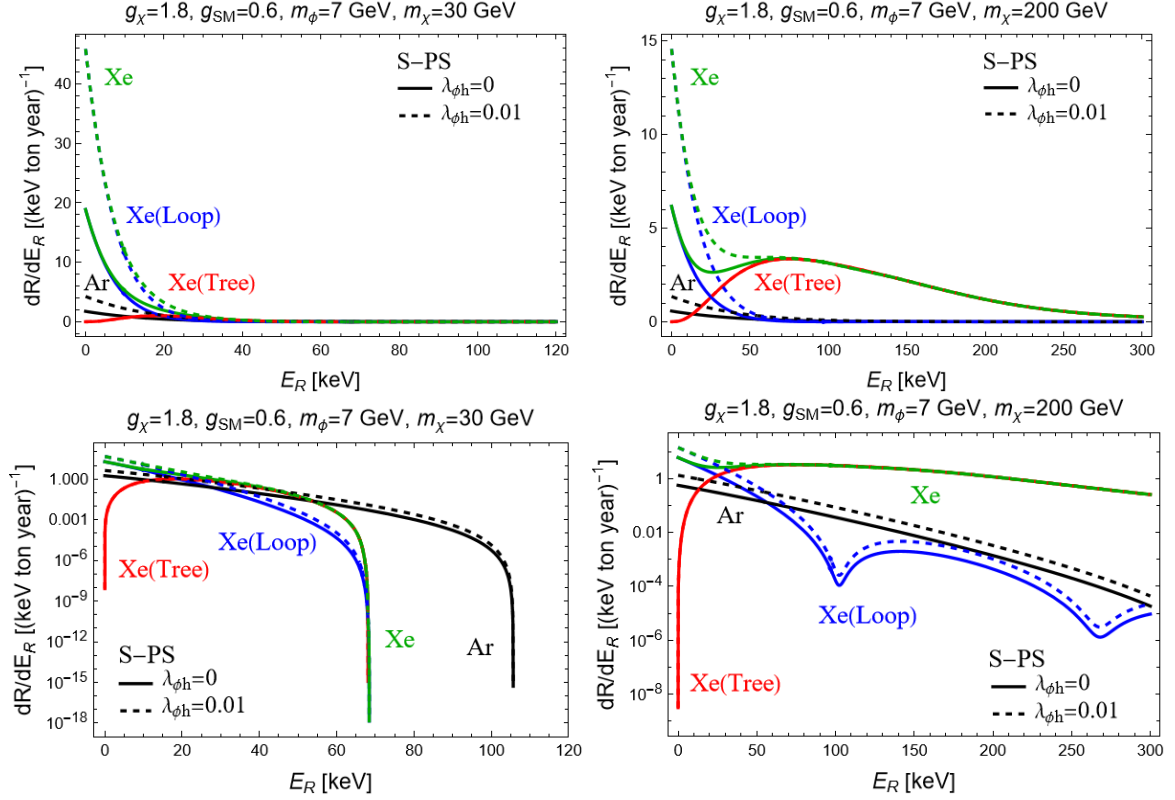


Figure 1. Differential event rates for S-PS Lagrangian couplings, with $g_\chi = 1.8$, $g_{\text{SM}} = 0.6$, $m_\phi = 7$ GeV, $m_\chi = 30$ GeV (left panels) and $m_\chi = 200$ GeV (right panels), $\lambda_{\phi h} = 0$ (solid lines) and $\lambda_{\phi h} = 0.01$ (dashed lines) for Ar (black lines) and Xe (green lines) targets. The contributions from tree-level only (red lines) and loop-level only (blue lines) in Xe are also shown. The rates are shown in linear scale in the upper panels and in logarithmic scale in the lower panels.

5 Comparison of Ar and Xe detection capability

Figures 1 and 2 show the predicted differential event rates for S-PS and PS-PS Lagrangian couplings, respectively, in Ar and Xe targets in linear and logarithmic scales. These figures show the tree-level only (red lines), loop-level contributions only (blue lines) and the total rate (green lines) in Xe, and the total rate entirely due to loop-level contributions (black lines) in Ar targets, for some values of the relevant parameters chosen as examples, i.e. $m_\phi = 7$ GeV, $g_\chi = 1.8$, $g_{\text{SM}} = 0.6$, the minimum and the maximum possible values of the ϕ - h coupling, $\lambda_{\phi h} = 0$ (solid lines) and $\lambda_{\phi h} = 0.01$ (dashed lines), and two values of the DM particle mass, $m_\chi = 30$ GeV and $m_\chi = 200$ GeV. The event rates have been computed using the Mathematica package `dmformfactor` [45]³.

Figures 1 and 2 clearly show that the loop-level contributions are important for low recoil energies, and that the expected rates for S-PS Lagrangian couplings are much larger, by a factor of about 10^2 , than those for PS-PS Lagrangian couplings. In both cases, the rates increase with $\lambda_{\phi h}$ by a factor of order 1 when going from the minimum to the maximum of

³Updated shell model one body density matrices for Ar and Xe are now available in the very recent open-source code [MuonBridge](#) [41].

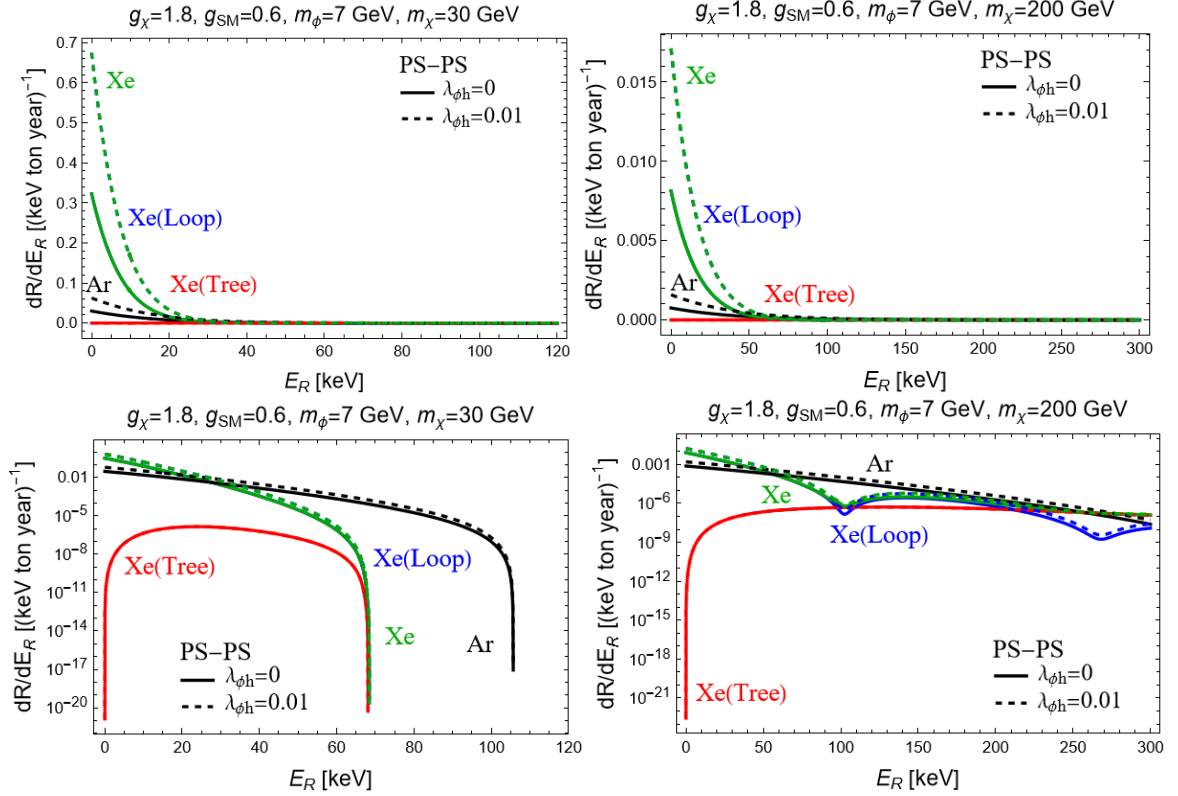


Figure 2. Same as figure 1 but for PS-PS Lagrangian couplings. Notice that the rates are roughly two orders of magnitude smaller than those in figure 1. The loop level contributions for Xe (blue lines) follow closely the total rate (green lines) and are therefore not clearly visible in the two top and the bottom left panels.

this coupling. Also in both cases, even at the lowest recoil energies, the rate expected in an Ar target is smaller by about one order of magnitude than in a Xe target.

To compare the detection capabilities of Ar and Xe-based detectors, we first consider idealized experimental conditions in which we ignore experimental backgrounds and efficiencies, and compute the event rates in each detector. Because loop-level contributions are only important at low energies, the energy threshold of future detectors will be very important for detecting rates enhanced by them. Although both argon and xenon-based detectors may achieve nuclear recoil energy thresholds below 1 keV using their S2 (ionization) signal only [11, 13, 60], in figure 3 we show lines of equal energy-integrated rates taking a threshold of 1 keV for both. This is the targeted threshold for future xenon-based detectors such as DARWIN/XLZD [7, 8] and for argon-based detectors such as DarkSide-LowMass (DS-LM) for [61]. We also consider the possibility of Ar-based detectors with a larger threshold, such as the 30 keV expected for DarkSide-20k [9] and show the corresponding lines of equal integrated rate in figure 4. Figure 3 shows lines of equal integrated rate above the threshold of $E_R = 1$ keV in the m_χ - g_χ plane, for Ar (left panel) and Xe (right panel) targets, for the most favorable type of Lagrangian coupling of the two we considered, the S-PS. The mediator mass is chosen to be $m_\phi = 7$ GeV, as in previous figures, and $\lambda_{ah} = 0$, which is one of the two values in previous figures. Lines corresponding to an integrated rate of 10 (dot-dashed lines above the solid lines), 1 (solid lines) and 0.1 (dashed lines below the solid lines) in units of

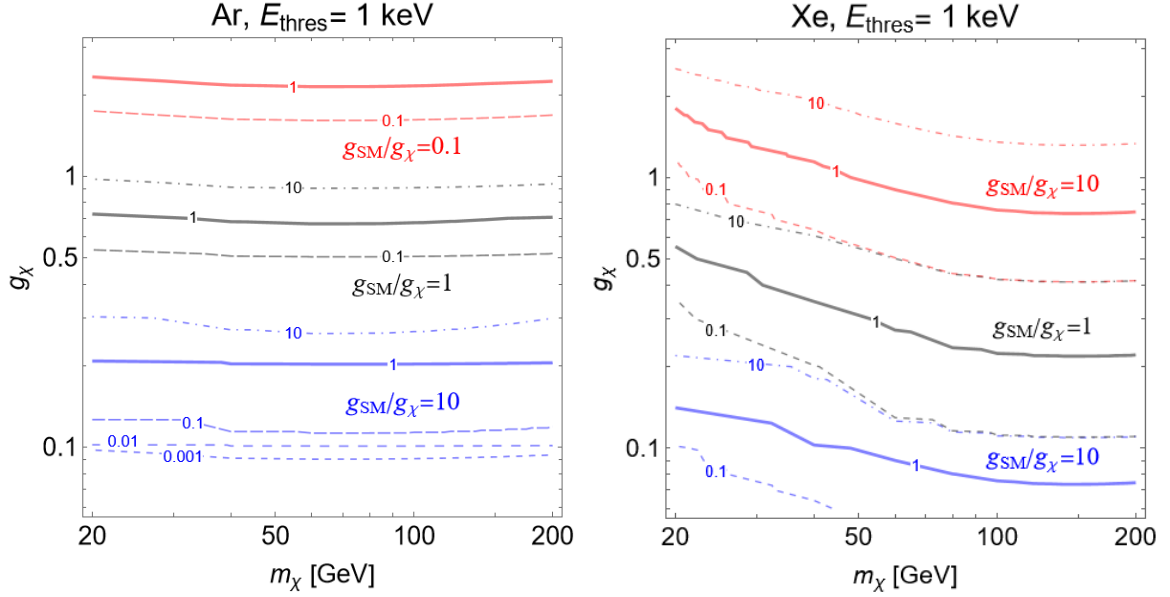


Figure 3. Lines of equal energy-integrated event rate for $E_R > 1$ keV in the m_χ - g_χ plane for Ar (left panel) and Xe (right panel) targets for a model with S-PS Lagrangian couplings, $m_\phi = 7$ GeV and $\lambda_{ah} = 0$, for three different values of the g_{SM}/g_χ coupling ratios, 0.1 (red lines), 1 (black lines) and 10 (blue lines). For each of these ratios different lines are shown corresponding to an integrated rate shown in the respective labels in units of $(\text{ton year})^{-1}$, e.g. 10 (dot-dashed lines above the solid lines), 1 (solid lines) and 0.1 (dashed lines below the solid lines).

$(\text{ton year})^{-1}$ are given for three different values of the g_{SM}/g_χ coupling ratios, 0.1 (in red), 1 (in black) and 10 (in blue). A few more blue lines corresponding to lower values of integrated rates, as labeled, are given for argon. Notice that we can integrate the total differential event rates (solid lines) in figure 1 above 1 keV to approximately obtain the value close to the red lines in figure 3 for $m_\chi = 30$ GeV and 200 GeV, $g_\chi = 1.8$ and $g_{\text{SM}}/g_\chi \simeq 0.3$.

Figure 3 allows us to estimate the difference in target mass between idealized argon- and xenon-based detectors that would be required to detect a similar number of events per year, if both have an energy threshold of 1 keV, for particular values of the parameters, assuming the same mediator mass as in the previous figures and m_χ in the 20 to 200 GeV range. For example, for a 30 GeV DM particle mass, $g_\chi = 0.2$, and $g_{\text{SM}} = 2$, the solid blue line in the left panel shows that an integrated rate of $1/(\text{ton year})$ is expected in Ar and the right panel the dot-dashed blue line indicates that $10/(\text{ton year})$ would be expected in Xe. Thus, to have a similar rate in both targets (ignoring backgrounds and efficiencies) one would require a 10 times larger mass in Ar than in Xe. The difference becomes more accentuated for larger DM masses, e.g. for a DM mass of 200 GeV, the rate in argon for the same coupling would still be close to $1/(\text{ton year})$, while in Xe the expected rate is $\gg 10/(\text{ton year})$ (curve not shown in the figure).

Figure 4 shows lines of equal integrated rate for an Ar target in the m_χ - g_χ plane for the same couplings and parameters used in figure 3 (i.e. for the S-PS Lagrangian coupling, with $m_\phi = 7$ GeV and $\lambda_{ah} = 0$), but above the threshold of $E_R = 30$ keV instead of 1 keV. This figure clearly shows the disadvantage that a larger energy threshold of 30 keV would have to detect DM particle with S-PS couplings in an Ar-based detector. This would make it practically impossible for Ar to detect this type of interaction. For example, for a 30 GeV

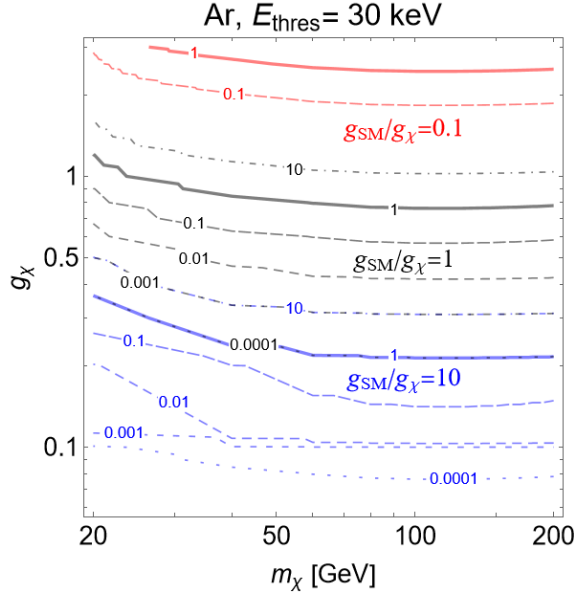


Figure 4. Same as figure 3, but only for Ar and assuming an energy threshold of $E_R = 30$ keV instead of 1 keV. Notice that the solid blue line corresponding to an integrated rate of $1/(\text{ton year})$ for $g_{\text{SM}}/g_\chi = 10$ is overlaid on the dotted black line corresponding to $0.0001/(\text{ton year})$ for $g_{\text{SM}}/g_\chi = 1$.

DM particle, $g_\chi = 0.2$, and $g_{\text{SM}} = 2$, the medium-dashed blue line in figure 4 shows that an integrated rate of between $0.01/(\text{ton year})$ and $0.1/(\text{ton year})$ is expected in Ar. This is more than an order of magnitude smaller than the rate expected in Ar with an energy threshold of 1 keV for the same couplings.

We do not present specific figures for the integrated rates in the PS-PS case. Our general conclusions comparing both targets would be similar to those for S-PS, but the event rates would be around two orders of magnitude smaller with respect to S-PS, requiring an experimental exposure of ~ 100 times larger to have a signal in the PS-PS case.

Next, we compare the detection capabilities of Ar- and Xe-based detectors in the context of realistic experimental conditions. For the Ar experiment, we choose the DS-LM proposal of the GADMC [62] for its low background level, in addition to its low energy threshold. Since the S1 pulse-shape electron-nuclear recoil type discrimination requires an energy deposit of about 30 keV to work [63, 64] –which is larger than typical energy deposits from loop-level rate contributions– we utilize the S2-only channel in this analysis, with a threshold of four electrons ($4e^-$). Here, we use the detector response model established in refs. [62, 65] to convert the true recoil energy spectrum into the number of electrons, and assume a total exposure of 1 ton year [62]. We adopt the background model from ref. [62], with three dominant background components considered: the detector γ scatters, ^{39}Ar β decays, and the solar neutrino coherent scatters. As the cut acceptance loss due to cuts other than the fiducialization cut is typically negligible for S2’s larger than a few electrons [60], we do not further consider the acceptance effect of those cuts throughout this analysis. We quantify the detector’s sensitivity to certain model parameters using the signal significance $\mathcal{S} = N_S/\sqrt{N_B}$, where N_S and N_B are the expected signal and background events, respectively. The significance heat map of models in the $m_\chi - g_\chi$ plane for S-PS interaction type with $m_\phi = 7$ GeV,

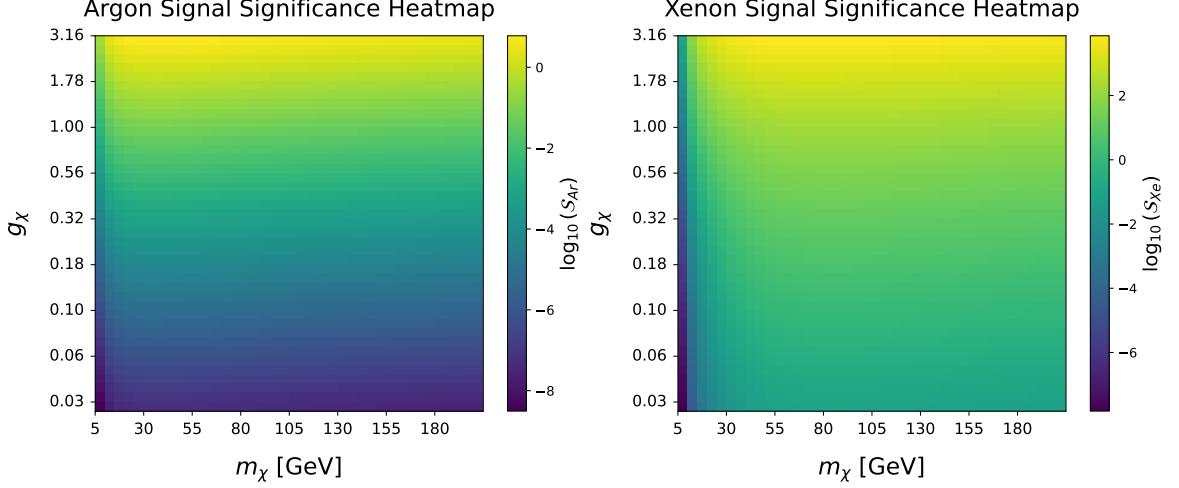


Figure 5. The signal significance, \mathcal{S} , heat map for the proposed DS-LM argon experiment (left) and the LZ xenon experiment (right). The model parameters assumed are $m_\phi = 7$ GeV, $\lambda_{\phi h} = 0.01$ and $g_{SM} = 0.6$ for S-PS Lagrangian couplings. As expected, in both target materials, the signal significances are larger at large DM couplings, indicating a better detection probability. The exposures being considered are 1 ton year for DS-LM [62] and 15.3 ton year for LZ [66]. \mathcal{S} in Ar grows faster with g_χ , as the entire rate comes from loop-level contributions with Lagrangian coefficients scaling as g_χ^2 . It also drops slower at smaller DM masses due to the fact that Ar is lighter than Xe.

$\lambda_{\phi h} = 0.01$, $g_{SM} = 0.06$, and m_χ in the 5 to 205 GeV range is shown in the left panel of figure 5.

For the Xe-based experiment, we use the LZ experiment [66] as a benchmark due to its leading sensitivity to nuclear recoil signatures and low background rate, with the detector configuration specified as in its first science run results [67]. We use NEST v2.3.11 [68] to simulate the detector response, with parameters adjusted to the calibration data in [67]. NEST simulated events in the S_1, S_2 space are then converted into the reconstructed energy using the relation $E_{rec} = W_q(S_1/g_1 + S_2/g_2)$, where $W_q = 13.7$ eV is the Xe work function, $g_1 = 0.114$ is the photon collection efficiency, and $g_2 = 47.1$ is the ionization gain [67]. The background model in the reconstructed energy space and cut acceptances for nuclear recoil signals are also adopted from ref. [67]. Most of the background components are electron-recoil-like, and Xe-based detectors are capable of discriminating between electron-recoils and nuclear-recoils at lower energy using S1/S2 ratio. This would further enhance the sensitivity of Xe-based detectors to low-energy nuclear-recoil signals for LZ. We conservatively assume a flat 99.5% electron-recoil rejection efficiency [66]. A total exposure of 15.3 ton year [66] is used to calculate the signal significance, \mathcal{S} , heat map for LZ. The result for the same model parameters we used for argon can be found in the right panel of figure 5.

From figure 5 we can see that for both the DS-LM argon and LZ xenon detectors, the largest signal significance is obtained for large g_χ values. Comparison of the two panels of the figure shows that for most of the parameter space, the signal significance for LZ is larger than that of DS-LM by a factor ranging from an order of magnitude to up to several orders of magnitude depending on m_χ and g_χ .

To better compare the detection capabilities of the two experiments, in figure 6 we show the signal significance \mathcal{S} ratio, between LZ and DS-LM. We note that this plot was created with a 15.3 ton year exposure assumption for LZ and 1 ton year for DS-LM. The

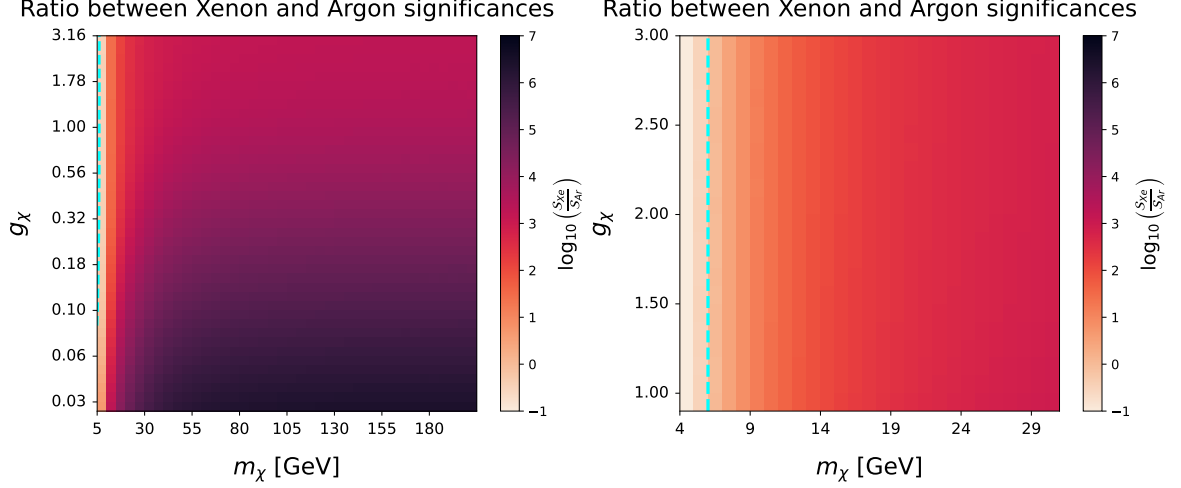


Figure 6. Left: The ratio of the LZ xenon and proposed DS-LM argon signal significances shown in figure 5, with the same detector configurations as in figure 5. Right: Zoom-in of the left panel to the region of lower DM mass and higher DM coupling that favors Ar-based experiments. For most part of the parameter space, the Xe-based experiment has a larger sensitivity than the Ar-based experiment. However, for a small corner of the parameter space, where m_χ is a few GeV and $g_\chi \sim 1 - 3$, the Ar-based experiment can reach ~ 10 times the sensitivity of Xe. The near vertical dashed cyan lines on both panels are where the Ar and Xe experiments are of the same sensitivity.

left panel shows this ratio for a large range of m_χ and g_χ values, while the right panel zooms in to the region of small m_χ and large g_χ values, where the \mathcal{S} ratio is the smallest. As $\mathcal{S} \propto (\text{exposure})^{1/2}$, in general it would take more time or fiducial mass for DS-LM to reach the same level of sensitivity as the LZ experiment. However, in cases where both the DM coupling is large ($g_\chi \sim 1 - 3$) and the DM is light (a few GeV), Ar-based experiments are favored, as shown in the right panel of figure 6. In the most favorable case for Ar, $\mathcal{S}_{Xe}/\mathcal{S}_{Ar} \sim 0.1$, and the DS-LM experiment can reach a sensitivity ~ 10 times better than the LZ experiment. In this case, we would need significantly more exposure in LZ to achieve a sensitivity similar to that of DS-LM.

6 Conclusions

In this work we have compared the capability of Ar and Xe based direct detection experiments for detecting fermionic DM candidates with interaction mediated by a spin-zero boson with pseudoscalar couplings to the SM fermions in the Lagrangian. At tree-level this type of coupling depends on the spin of the target nucleus and thus would not be detectable in an argon target, since Ar does not have spin. We considered a minimal extension of the simple one mediator model which allows us to compute loop-level contributions to the direct detection event rate that are independent of the nuclear spin. These contributions are very important at low recoil energies and thus a low energy threshold is essential to detect them.⁴

⁴After completing our work, we noticed ref. [69], which deals with isospin-violation in DM couplings and compares the Xe and Ar sensitivity to SD ($\vec{S}_\chi \cdot \vec{S}_N$) interactions (due to a $\bar{f}\gamma_\mu\gamma_5 f$ coupling to SM fermions) within two effective SM gauge-invariant models. It finds that Ar becomes sensitive to it at low E_R , due to an $\mathcal{O}_8 = (\vec{S}_\chi \cdot v^T)1_N$ operator (v^T is the transverse DM velocity) imposed by gauge invariance.

Considering idealized experimental conditions for the two detectors, we showed that with a comparably low energy threshold close to 1 keV, an Ar-based detector could have a similar integrated rate as a Xe-based detector if its exposure is 10 or more times larger than a Xe detector. Considering more realistic experimental conditions based on the DS-LM experiment for Ar and LZ for Xe, we found that in general for large DM masses and small DM couplings we need many times the proposed exposure in the Ar-based DS-LM experiment to reach a sensitivity similar to that of the Xe-based LZ experiment. However, in a small region of the parameter space, where the DM mass is small (a few GeV) and the DM coupling is large ($g_\chi \sim 1 - 3$), the Ar-based experiment is favored and can reach a sensitivity which is ~ 10 times better than the Xe-based experiment.

Acknowledgements

NB acknowledges the support of the Natural Sciences and Engineering Research Council of Canada (NSERC), funding reference number RGPIN-2020-07138, the NSERC Discovery Launch Supplement, DGECR-2020-00231, and the Canada Research Chairs Program. GG was supported in part by the Department of Energy under Award Number DE-SC0009937. MC was supported in part by the Department of Energy under Award Number DE-SC000993, and by the World Premier International Research Center Initiative (WPI) MEXT, Japan. ACK and YX were supported in part by the U.S. Department of Energy, Office of Science, Office of High Energy Physics under Award Number DE-SC0025629.

References

- [1] **XENON** Collaboration, E. Aprile et al., *Constraining the spin-dependent WIMP-nucleon cross sections with XENON1T*, *Phys. Rev. Lett.* **122** (2019), no. 14 141301, [[arXiv:1902.03234](#)].
- [2] **XENON** Collaboration, E. Aprile et al., *Projected WIMP sensitivity of the XENONnT dark matter experiment*, *JCAP* **11** (2020) 031, [[arXiv:2007.08796](#)].
- [3] **LZ** Collaboration, D. S. Akerib et al., *Projected WIMP sensitivity of the LUX-ZEPLIN dark matter experiment*, *Phys. Rev. D* **101** (2020), no. 5 052002, [[arXiv:1802.06039](#)].
- [4] **LZ** Collaboration, D. S. Akerib et al., *The LUX-ZEPLIN (LZ) Experiment*, *Nucl. Instrum. Meth. A* **953** (2020) 163047, [[arXiv:1910.09124](#)].
- [5] **PandaX** Collaboration, H. Zhang et al., *Dark matter direct search sensitivity of the PandaX-4T experiment*, *Sci. China Phys. Mech. Astron.* **62** (2019), no. 3 31011, [[arXiv:1806.02229](#)].
- [6] **PandaX-4T** Collaboration, Y. Meng et al., *Dark Matter Search Results from the PandaX-4T Commissioning Run*, *Phys. Rev. Lett.* **127** (2021), no. 26 261802, [[arXiv:2107.13438](#)].
- [7] L. Baudis, *DARWIN/XLZD: A future xenon observatory for dark matter and other rare interactions*, *Nucl. Phys. B* **1003** (2024) 116473, [[arXiv:2404.19524](#)].
- [8] J. Aalbers, K. Abe, M. Adrover, S. A. Maouloud, D. Akerib, A. Al Musalhi, F. Alder, L. Althueser, D. Amaral, C. Amarasinghe, et al., *The xlzd design book: Towards the next-generation liquid xenon observatory for dark matter and neutrino physics*, *arXiv preprint arXiv:2410.17137* (2024).
- [9] **DarkSide-20k** Collaboration, C. E. Aalseth et al., *DarkSide-20k: A 20 tonne two-phase LAr TPC for direct dark matter detection at LNGS*, *Eur. Phys. J. Plus* **133** (2018) 131, [[arXiv:1707.08145](#)].

- [10] **ArDM** Collaboration, J. Calvo et al., *Backgrounds and pulse shape discrimination in the ArDM liquid argon TPC*, *JCAP* **12** (2018) 011, [[arXiv:1712.01932](#)].
- [11] **DarkSide-50** Collaboration, P. Agnes et al., *Search for low mass dark matter in DarkSide-50: the bayesian network approach*, *Eur. Phys. J. C* **83** (2023) 322, [[arXiv:2302.01830](#)].
- [12] **DarkSide-20k** Collaboration, I. Manthos, *DarkSide-20k: Next generation Direct Dark Matter searches with liquid Argon*, *PoS EPS-HEP2023* (2024) 113, [[arXiv:2312.03597](#)].
- [13] J. Aalbers et al., *A next-generation liquid xenon observatory for dark matter and neutrino physics*, *J. Phys. G* **50** (2023), no. 1 013001, [[arXiv:2203.02309](#)].
- [14] W. M. Bonivento and F. Terranova, *The science and technology of liquid argon detectors*, [arXiv:2405.01153](#).
- [15] **DARWIN** Collaboration, J. Aalbers et al., *DARWIN: towards the ultimate dark matter detector*, *JCAP* **11** (2016) 017, [[arXiv:1606.07001](#)].
- [16] C. Galbiati, “Direct dark matter detection with noble gases.” Talk at the UCLA Dark Matter 2018 Conference.
- [17] **DarkSide 20k** Collaboration, P. Agnes et al., *Sensitivity of future liquid argon dark matter search experiments to core-collapse supernova neutrinos*, *JCAP* **03** (2021) 043, [[arXiv:2011.07819](#)].
- [18] G. B. Gelmini, V. Takhistov, and S. J. Witte, *Casting a Wide Signal Net with Future Direct Dark Matter Detection Experiments*, *JCAP* **07** (2018) 009, [[arXiv:1804.01638](#)]. [Erratum: *JCAP* **02**, E02 (2019)].
- [19] G. Arcadi, M. Lindner, F. S. Queiroz, W. Rodejohann, and S. Vogl, *Pseudoscalar Mediators: A WIMP model at the Neutrino Floor*, *JCAP* **03** (2018) 042, [[arXiv:1711.02110](#)].
- [20] N. F. Bell, G. Busoni, and I. W. Sanderson, *Loop Effects in Direct Detection*, *JCAP* **08** (2018) 017, [[arXiv:1803.01574](#)]. [Erratum: *JCAP* **01**, E01 (2019)].
- [21] T. Li, *Revisiting the direct detection of dark matter in simplified models*, *Phys. Lett. B* **782** (2018) 497–502, [[arXiv:1804.02120](#)].
- [22] T. Abe, M. Fujiwara, and J. Hisano, *Loop corrections to dark matter direct detection in a pseudoscalar mediator dark matter model*, *JHEP* **02** (2019) 028, [[arXiv:1810.01039](#)].
- [23] F. Ertas and F. Kahlhoefer, *Loop-induced direct detection signatures from CP-violating scalar mediators*, *JHEP* **06** (2019) 052, [[arXiv:1902.11070](#)].
- [24] M. Freytsis and Z. Ligeti, *On dark matter models with uniquely spin-dependent detection possibilities*, *Phys. Rev. D* **83** (2011) 115009, [[arXiv:1012.5317](#)].
- [25] K. R. Dienes, J. Kumar, B. Thomas, and D. Yaylali, *Overcoming Velocity Suppression in Dark-Matter Direct-Detection Experiments*, *Phys. Rev. D* **90** (2014), no. 1 015012, [[arXiv:1312.7772](#)].
- [26] C. Boehm, M. J. Dolan, C. McCabe, M. Spannowsky, and C. J. Wallace, *Extended gamma-ray emission from Coy Dark Matter*, *JCAP* **05** (2014) 009, [[arXiv:1401.6458](#)].
- [27] S. Ipek, D. McKeen, and A. E. Nelson, *A Renormalizable Model for the Galactic Center Gamma Ray Excess from Dark Matter Annihilation*, *Phys. Rev. D* **90** (2014), no. 5 055021, [[arXiv:1404.3716](#)].
- [28] J. M. No, *Looking through the pseudoscalar portal into dark matter: Novel mono-Higgs and mono-Z signatures at the LHC*, *Phys. Rev. D* **93** (2016), no. 3 031701, [[arXiv:1509.01110](#)].
- [29] D. Goncalves, P. A. N. Machado, and J. M. No, *Simplified Models for Dark Matter Face their Consistent Completions*, *Phys. Rev. D* **95** (2017), no. 5 055027, [[arXiv:1611.04593](#)].

- [30] M. Bauer, U. Haisch, and F. Kahlhoefer, *Simplified dark matter models with two Higgs doublets: I. Pseudoscalar mediators*, *JHEP* **05** (2017) 138, [[arXiv:1701.07427](#)].
- [31] M. Bauer, M. Klassen, and V. Tenorth, *Universal properties of pseudoscalar mediators in dark matter extensions of 2HDMs*, *JHEP* **07** (2018) 107, [[arXiv:1712.06597](#)].
- [32] **LHC Dark Matter Working Group** Collaboration, T. Abe et al., *LHC Dark Matter Working Group: Next-generation spin-0 dark matter models*, *Phys. Dark Univ.* **27** (2020) 100351, [[arXiv:1810.09420](#)].
- [33] G. D’Ambrosio, G. F. Giudice, G. Isidori, and A. Strumia, *Minimal flavor violation: An Effective field theory approach*, *Nucl. Phys. B* **645** (2002) 155–187, [[hep-ph/0207036](#)].
- [34] F. Bishara, J. Brod, B. Grinstein, and J. Zupan, *Renormalization Group Effects in Dark Matter Interactions*, *JHEP* **03** (2020) 089, [[arXiv:1809.03506](#)].
- [35] G. Passarino and M. J. G. Veltman, *One Loop Corrections for $e^+ e^-$ Annihilation Into $\mu^+ \mu^-$ in the Weinberg Model*, *Nucl. Phys. B* **160** (1979) 151–207.
- [36] T. Abe and R. Sato, *Quantum corrections to the spin-independent cross section of the inert doublet dark matter*, *JHEP* **03** (2015) 109, [[arXiv:1501.04161](#)].
- [37] H. H. Patel, *Package-X: A Mathematica package for the analytic calculation of one-loop integrals*, *Comput. Phys. Commun.* **197** (2015) 276–290, [[arXiv:1503.01469](#)].
- [38] H. H. Patel, *Package-X 2.0: A Mathematica package for the analytic calculation of one-loop integrals*, *Comput. Phys. Commun.* **218** (2017) 66–70, [[arXiv:1612.00009](#)].
- [39] A. Denner, S. Dittmaier, and L. Hofer, *Collier: a fortran-based Complex One-Loop Library in Extended Regularizations*, *Comput. Phys. Commun.* **212** (2017) 220–238, [[arXiv:1604.06792](#)].
- [40] F. Bishara, J. Brod, B. Grinstein, and J. Zupan, *From quarks to nucleons in dark matter direct detection*, *JHEP* **11** (2017) 059, [[arXiv:1707.06998](#)].
- [41] W. Haxton, K. McElvain, T. Menzo, E. Rule, and J. Zupan, *Effective theory tower for $\mu \rightarrow e$ conversion*, [[arXiv:2406.13818](#)].
- [42] J. Fan, M. Reece, and L.-T. Wang, *Non-relativistic effective theory of dark matter direct detection*, *JCAP* **11** (2010) 042, [[arXiv:1008.1591](#)].
- [43] A. L. Fitzpatrick, W. Haxton, E. Katz, N. Lubbers, and Y. Xu, *The Effective Field Theory of Dark Matter Direct Detection*, *JCAP* **02** (2013) 004, [[arXiv:1203.3542](#)].
- [44] A. L. Fitzpatrick, W. Haxton, E. Katz, N. Lubbers, and Y. Xu, *Model Independent Direct Detection Analyses*, [[arXiv:1211.2818](#)].
- [45] N. Anand, A. L. Fitzpatrick, and W. C. Haxton, *Weakly interacting massive particle-nucleus elastic scattering response*, *Phys. Rev. C* **89** (2014), no. 6 065501, [[arXiv:1308.6288](#)].
- [46] J. B. Dent, L. M. Krauss, J. L. Newstead, and S. Sabharwal, *General analysis of direct dark matter detection: From microphysics to observational signatures*, *Phys. Rev. D* **92** (2015), no. 6 063515, [[arXiv:1505.03117](#)].
- [47] A. K. Drukier, K. Freese, and D. N. Spergel, *Detecting Cold Dark Matter Candidates*, *Phys. Rev. D* **33** (1986) 3495–3508.
- [48] N. Bozorgnia, F. Calore, M. Schaller, M. Lovell, G. Bertone, C. S. Frenk, R. A. Crain, J. F. Navarro, J. Schaye, and T. Theuns, *Simulated milky way analogues: implications for dark matter direct searches*, *JCAP* **05** (2016) 024, [[arXiv:1601.04707](#)].
- [49] C. Kelso, C. Savage, M. Valluri, K. Freese, G. S. Stinson, and J. Bailin, *The impact of baryons on the direct detection of dark matter*, *JCAP* **08** (2016) 071, [[arXiv:1601.04725](#)].

- [50] J. D. Sloane, M. R. Buckley, A. M. Brooks, and F. Governato, *Assessing astrophysical uncertainties in direct detection with galaxy simulations*, *Astrophys.J.* **831** (2016) 93, [[arXiv:1601.05402](#)].
- [51] R. Poole-McKenzie, A. S. Font, B. Boxer, I. G. McCarthy, S. Burdin, S. G. Stafford, and S. T. Brown, *Informing dark matter direct detection limits with the ARTEMIS simulations*, *JCAP* **11** (2020) 016, [[arXiv:2006.15159](#)].
- [52] J. Reynoso-Cordova, N. Bozorgnia, and M.-C. Piro, *The Large Magellanic Cloud: expanding the low-mass parameter space of dark matter direct detection*, *JCAP* **12** (2024) 037, [[arXiv:2409.09119](#)].
- [53] A. Smith-Orlik et al., *The impact of the Large Magellanic Cloud on dark matter direct detection signals*, *JCAP* **10** (2023) 070, [[arXiv:2302.04281](#)].
- [54] G. Besla, A. Peter, and N. Garavito-Camargo, *The highest-speed local dark matter particles come from the Large Magellanic Cloud*, *JCAP* **11** (2019) 013, [[arXiv:1909.04140](#)].
- [55] K. Donaldson, M. S. Petersen, and J. Peñarrubia, *Effects on the local dark matter distribution due to the large magellanic cloud*, *Mon. Not. Roy. Astron. Soc.* **513** (2022), no. 1 46–51, [[arXiv:2111.15440](#)].
- [56] M. J. Reid et al., *Trigonometric Parallaxes of Massive Star Forming Regions: VI. Galactic Structure, Fundamental Parameters and Non-Circular Motions*, *Astrophys. J.* **700** (2009) 137–148, [[arXiv:0902.3913](#)].
- [57] J. Bovy, D. W. Hogg, and H.-W. Rix, *Galactic masers and the Milky Way circular velocity*, *Astrophys. J.* **704** (2009) 1704–1709, [[arXiv:0907.5423](#)].
- [58] M. C. Smith et al., *The RAVE Survey: Constraining the Local Galactic Escape Speed*, *Mon. Not. Roy. Astron. Soc.* **379** (2007) 755–772, [[astro-ph/0611671](#)].
- [59] R. Schoenrich, J. Binney, and W. Dehnen, *Local Kinematics and the Local Standard of Rest*, *Mon. Not. Roy. Astron. Soc.* **403** (2010) 1829, [[arXiv:0912.3693](#)].
- [60] **DarkSide** Collaboration, P. Agnes et al., *Low-Mass Dark Matter Search with the DarkSide-50 Experiment*, *Phys. Rev. Lett.* **121** (2018), no. 8 081307, [[arXiv:1802.06994](#)].
- [61] **Global Argon Dark Matter** Collaboration, M. Wada, *DarkSide-LowMass: Sensitivity Projections for a New Detector Designed for Light Dark Matter Searches*, *PoS TAUP2023* (2024) 057.
- [62] **Global Argon Dark Matter** Collaboration, P. Agnes et al., *Sensitivity projections for a dual-phase argon TPC optimized for light dark matter searches through the ionization channel*, *Phys. Rev. D* **107** (2023), no. 11 112006, [[arXiv:2209.01177](#)].
- [63] A. Fan, *Results from the DarkSide-50 Dark Matter Experiment*. PhD thesis, UCLA, 2016.
- [64] M. Cadeddu, *DarkSide-20k sensitivity, directional dark matter detection and the role of coherent elastic neutrino-nucleus scattering background*. PhD thesis, Cagliari U., 2018.
- [65] **DarkSide** Collaboration, P. Agnes et al., *Calibration of the liquid argon ionization response to low energy electronic and nuclear recoils with DarkSide-50*, *Phys. Rev. D* **104** (2021), no. 8 082005, [[arXiv:2107.08087](#)].
- [66] B. J. Mount et al., *LUX-ZEPLIN (LZ) Technical Design Report*, [[arXiv:1703.09144](#)].
- [67] **LZ** Collaboration, J. Aalbers et al., *First Dark Matter Search Results from the LUX-ZEPLIN (LZ) Experiment*, *Phys. Rev. Lett.* **131** (2023), no. 4 041002, [[arXiv:2207.03764](#)].
- [68] M. Szydagis, N. Barry, K. Kazkaz, J. Mock, D. Stolp, M. Sweany, M. Tripathi, S. Uvarov, N. Walsh, and M. Woods, *NEST: A Comprehensive Model for Scintillation Yield in Liquid Xenon*, *JINST* **6** (2011) P10002, [[arXiv:1106.1613](#)].

- [69] A. Cheek, D. D. Price, and E. M. Sanford, *Isospin-violating dark matter at liquid noble detectors: new constraints, future projections, and an exploration of target complementarity*, *Eur. Phys. J. C* **83** (2023), no. 10 914, [[arXiv:2302.05458](#)].